Numerical characterisation of the rotational behaviour of grey cast iron tunnel joints

Agustín Ruiz López [*], Aikaterini Tsiampousi, Jamie R. Standing, David M. Potts

Imperial College London, Department of Civil and Environmental Engineering, London, UK

A R T I C L E   I N F O

Keywords:
Grey cast iron
Segmental lining
Tunnel joints
Rotational stiffness

A B S T R A C T

The structural assessment of segmental grey cast iron (GCI) tunnel linings to nearby construction is challenging due to the presence of the joints affecting the stiffness of the tunnel lining. This paper presents an extensive investigation, using 3D finite element (FE) analyses, into the bending moment-rotation (M-θ) behaviour of two GCI tunnel joint geometries. These two geometries correspond to standard running and station tunnels of the London Underground network. The contribution of this study is two-fold. i) The novel characterisation of the M-θ response enables the development of new models for simulating the mechanical response of GCI tunnel joints with structural elements which can be used in simplified, 2D geotechnical analysis for tunnel safety assessments. ii) The analyses provide insight into the behaviour of GCI tunnel linings that would be difficult to achieve through experimental and field observations alone. More specifically, the analyses show that when the bolts are removed from the joints the possibility of tensile failure can be disregarded; that the initial bolt preload influences the rotational stiffness only after some rotation has taken place and does not alter the bending moment of opening; and that the out-of-plane displacement restraint has little influence on the joint response.

1. Introduction

There are hundreds of kilometres of tunnels of the London Underground (LU) network lined with grey cast iron (GCI) tunnel linings. These are segmental linings that comprise rings and segments bolted together at their circumferential and longitudinal joints, respectively. A typical GCI ring for a running tunnel of the LU network is shown in Fig. 1 with annotations of the terms adopted throughout this paper. It is well understood that the structural response of GCI tunnel linings, and segmental tunnel linings in general, largely depends on the response of the joints. Thus, an adequate characterisation of the stiffness of the joints is essential for a meaningful evaluation of a tunnel's current internal forces and its response to new solicitations, which is becoming ever more relevant as the underground space becomes progressively more congested in urban areas.

Although only a small number of investigations has been conducted, previous laboratory works provided many valuable insights into the behaviour of GCI longitudinal joints. Thomas (1977) performed bending tests on two half segments of a 12 ft 7 in internal diameter GCI tunnel bolted together at the longitudinal joint. The joint was subjected to a bending load whereas the (circumferential) axial force remained equal

to zero throughout the test. Only positive bending (i.e., that causing tension at the intrados of the tunnel lining) was considered. It was observed that the joint opening was larger towards the edge of the circumferential flange than at the middle location and that the change in force of the outer bolts was approximately twice as large as that of the middle bolt throughout the test. The joint developed a large rotation (about 2° or 0.035 rad by the end of the test) without apparent signs of failure of the segments or the bolts. Tsiampousi et al. (2017) reported on a series of two-segment tests on half-scale GCI segments following the same set-up employed by Thomas (1977), which were part of a wider laboratory investigation conducted at Imperial College London that involved structural tests on a segmental GCI ring (Yu et al., 2017; Afshan et al., 2017). Thanks to an extensive instrumentation system, the tests enabled Thomas' (1977) observations in relation to the uneven behaviour of the joint to be confirmed quantitatively. Even though the two investigations provided relevant insights into the response of GCI tunnel joints, the tests were performed under zero axial force and so did not represent field conditions adequately; furthermore, only the behaviour under positive bending was studied. The experimental tests on the segmental GCI ring, where the latter was subjected to small distortion levels (Yu et al., 2017), showed that the stiffness of the joints is not too

* Corresponding author at: Imperial College London, Dpt. of Civil and Environmental Engineering, Skempton Building, London SW7 2AZ, UK.
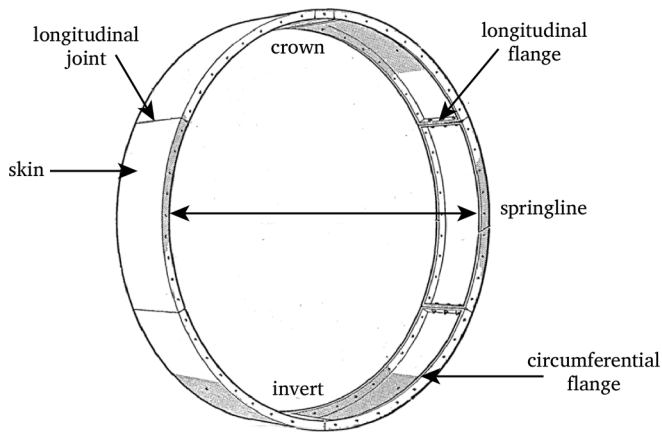 *E-mail address:* a.ruiz-lopez17@imperial.ac.uk (A. Ruiz López).

Fig. 1. GCI ring of a standard running tunnel in the LU network with adopted terminology (adapted from Thomas, 1974).

different from that of other segment cross-sections while the joints remain closed and that the influence of the bolt preload on the bending moment of opening is negligible when the joint is under compression. However, the tests where the ring was subjected to large distortion levels (Afshan et al., 2017) illustrated that the action of the bolts beyond the onset of opening is significant. In the second of these tests, a fracture occurred at the circumferential flange just next to one of the longitudinal joints subjected to positive bending and extended from the intrados to the skin; the test was interrupted right after this occurred so that the joint response after fracturing was not investigated. Even though the testing programme on the segmental ring provided useful findings, the internal forces acting at the joints could not be monitored and so the M-θ response of the joints was not characterised.

The behaviour of concrete longitudinal joints has been investigated more extensively in the laboratory (Hordijk & Gijsbers, 1996; Li et al.,

2015, Jin et al., 2017). Hordijk & Gijsbers (1996) conducted a detailed investigation where bending tests under six different axial force levels, kept constant throughout the tests, were performed. The M-θ curves obtained were approximately linear up to the opening of the joint and exhibited a gradual degradation in stiffness up to the end of their capacity. The dependency of the M-θ response on the compression level was obvious: the bending moment of joint opening and the initial stiffness both increased with applied axial force.

Several mechanical models have been proposed to predict the behaviour of concrete tunnel joints. Janssen (1983) proposed a model where the joint is represented with an equivalent beam and the action of bolts is neglected, and which assumes a linear stress–strain response in compression and that the beam cannot sustain any tensile stresses. The model predicts a linear rotational stiffness while the joint is closed and a nonlinear stiffness decay after joint opening. The predicted M-θ curve converges asymptotically towards the bending moment at maximum eccentricity. Hordijk & Gijsbers (1996) showed that Janssen's (1983) model produce a reasonable agreement with their experimental M-θ curves for the different axial force levels. Blom (2002) and Tvede-Jensen et al. (2017) proposed modifications to the Janssen model adopting a bilinear and parabolic stress–strain relationships in compression, respectively. Li et al. (2015) also built on the concepts proposed by Janssen (1983) to develop a mechanical model that considered a non-symmetric joint cross-section and the action of bolts. Nevertheless, these mechanical models do not consider the non-uniform rotation along the joint width that is observed in GCI tunnel joints under positive bending nor the associated uneven bolt action.

Regarding previous numerical investigations looking at the behaviour of GCI joints, Li et al. (2014) simulated the two-segment test conducted by Thomas (1977) using a 3D model that adopted solid elements for the segments and interface elements for the contact between segments. The numerical results matched reasonably well the response of the laboratory test. Tsiampousi et al. (2017) performed a series of numerical analyses alongside their laboratory investigation with a 3D model similar to that of Li et al. (2014). The authors performed a careful
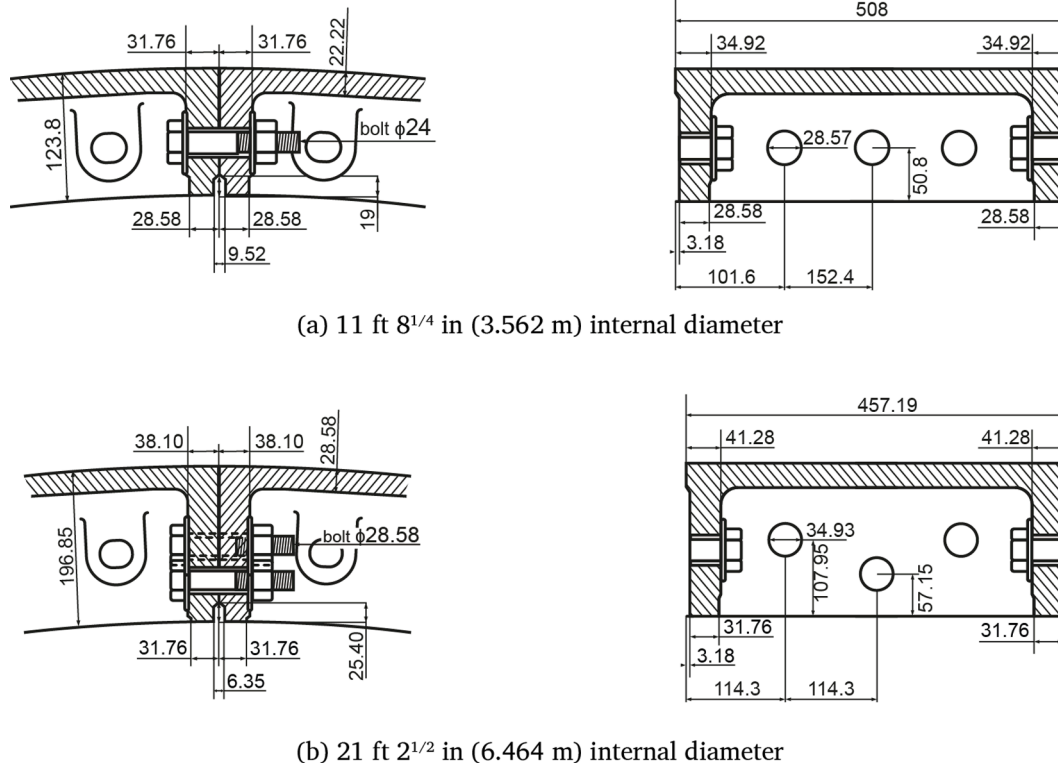

(a) 11 ft 8^{1/4} in (3.562 m) internal diameter

(b) 21 ft 2^{1/2} in (6.464 m) internal diameter

Fig. 2. Tunnel joint geometries considered in the numerical investigation. Longitudinal view on the left, circumferential view on the right. All dimensions in mm.
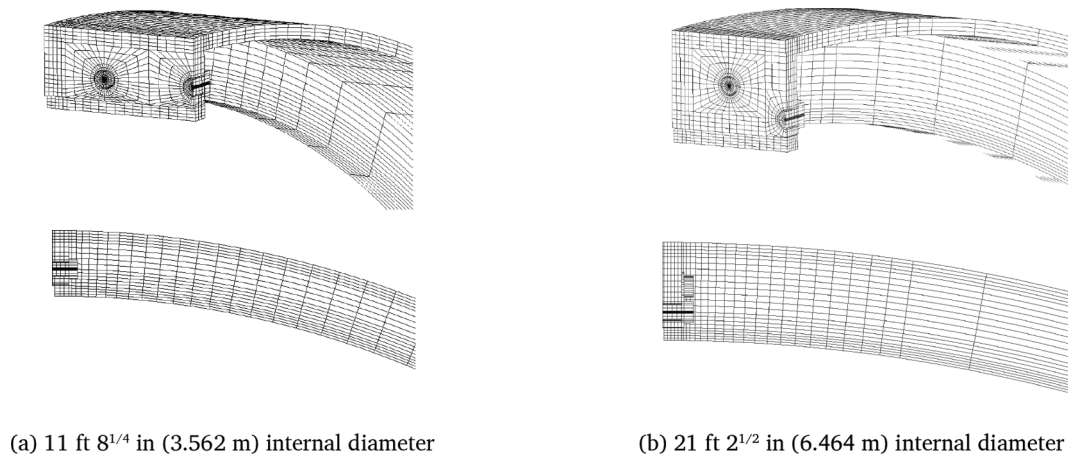
(a) 11 ft 8$^{1/4}$ in (3.562 m) internal diameter

(b) 21 ft 2$^{1/2}$ in (6.464 m) internal diameter

Fig. 3. Finite element meshes employed in the analyses.

calibration of the stiffness of the interface elements and the bolting system in order to capture the laboratory response. These two numerical investigations established the methodologies required to reproduce adequately the joint behaviour but did not attempt a full characterisation of the M-θ response of GCI joints.

In this paper, the rotational behaviour of GCI longitudinal joints is evaluated in a 3D numerical investigation using the Imperial College Finite Element Program ICFEP (Potts & Zdravkovic, 1999). First, the behaviour of two joint geometries corresponding to prototype running and station tunnels of the LU network is extensively characterised. Each joint geometry is analysed under positive and negative bending subjected to a range of axial force levels covering those expected in the field. The primary outcome of these analyses is the derivation of a series of M-θ curves extending up to ultimate conditions for each geometry and bending mode. These pave the way for the development of new constitutive models (Ruiz López et al., 2022b). Subsequently, the impact of removing the bolts from the joints, the bolt preload magnitudes and the out-of-plane restraint condition on the rotational behaviour are assessed through additional analyses, providing useful insight into the global behaviour of bolted segmental GCI tunnel linings, which would be difficult and expensive to achieve in laboratory and field experiments alone.

2. Selection of joint geometries

The rotational behaviour of the longitudinal joints of two GCI tunnel geometries is investigated in this paper: the 11 ft 8$^{1/4}$ in (3.562 m) internal diameter running tunnel geometry and the 21 ft 2$^{1/2}$ in (6.464 m) internal diameter station tunnel geometry. Fig. 2 presents the geometry and dimensions of the two tunnel joint geometries. Assessment of a detailed breakdown of GCI ring geometries of tunnel sections of the Bakerloo Line, Central Line, Victoria Line and Waterloo and City Line, facilitated by TfL (2020), revealed that 11 ft 8$^{1/4}$ in, the 12 ft 6 in and the 12 ft 0 in are the most common diameters for running tunnels. The joint geometries from these tunnels are identical and so the behaviour of the 11 ft 8$^{1/4}$ in geometry is representative of that of the other tunnel diameters. Among the larger tunnels, the 21 ft 2$^{1/2}$ in and the 25 ft 0 in are the most common diameters for station and cross-over tunnels, respectively. The joint geometries of the larger tunnels have their middle bolt in the longitudinal joint offset towards the intrados with respect to the outer bolts, as shown in Fig. 2b, which results in significantly different response of the bolts as compared to that of the running tunnel joints. In addition to the two geometries considered here, Ruiz López (2022) also investigated the behaviour of the 12 ft 6 in joint geometry without the caulking groove and the 25 ft 0 in, which behaved qualitatively similar in most respects to the joints of the 11 ft 8$^{1/4}$ in and the 21 ft 2$^{1/2}$ in linings, respectively.

3. Description of the numerical model

A quarter of a ring with a single joint positioned at the crown was considered in the analyses. This model geometry was deemed convenient to analyse the joint behaviour and did not aim to represent an actual tunnel ring (Fig. 1). Only half the segment width was included taking advantage of symmetry. Fig. 3 depicts the mesh discretisation of the longitudinal joint corresponding to the 11 ft 8$^{1/4}$ in and the 21 ft 2$^{1/2}$ in tunnel geometries. 20-noded solid elements and 16-noded interface elements (Day & Potts, 1994) were employed. Physical compatibility was assumed between the different components of the bolting system (bolt, nut and washer) and between the washer and the flange. Ruiz López et al. (2022a) adopted this approach with a reduced bolt stiffness value and successfully reproduced the behaviour of the longitudinal joint as observed experimentally.

Regarding the applied boundary conditions, the displacements normal to the symmetry planes, i.e. at the crown, springline and circumferentially along the middle of the segment, were restrained. At the crown, where the joint was situated, the displacements were restrained in the outer surface of the interface elements whereas the inner surface (that attached to the solid elements) was allowed to deform freely hence, allowing opening of the joint. The displacements normal to the circumferential flange were also fixed mimicking the restriction provided by adjacent rings in the field. The influence of the latter boundary condition on the rotational response is discussed in Section 7.3 and compared with only restricting the upper height of the flange.

The loading sequence comprised three steps. First, the bolt preload was applied via a tensile stress acting on the exposed face of the threads at the crown symmetry plane; the displacements normal to the exposed face of the threads were fixed in subsequent loading increments. The magnitude of the bolt preload was set as 25% of the tensile load of the bolt at yield which was adopted based on the laboratory measurements of bolt preloads reported by Tsiampousi et al. (2017). A sensitivity study on the influence of the bolt preload on the joint rotational response is presented in Section 7.2. Subsequently to the bolt preload, the ring was subjected to a circumferential axial compression via a normal stress applied around the extrados of the ring. Analyses with normal stresses corresponding to tunnel depths of 6 m, 12 m, 24 m and 48 m were conducted assuming that the full overburden pressure is acting on the tunnel lining and a soil unit weight γ of 20 kN/m^3. The normal stresses remained constant throughout the analysis. GCG (2002) reported that about 70% of the running tunnels of the Northern, Jubilee and Piccadilly Lines have a ground cover between 6 m and 24 m while about 20% have a cover between 24 m and 40 m. Correspondingly, the range of tunnel depths considered (6–48 m) in the investigation covered the depth of the vast majority of (running) tunnels of the LU network. It is worth noting that field measurements (Ward & Thomas, 1965) indicate that the

Table 1
Material parameters for GCI.

Model parameters	Value
Elastic modulus E	100 GPa
Poisson's ratio μ	0.26
Tensile yield strength f_{ty}	40 MPa
Tensile peak strength f_{tp}	140 MPa
Tensile ultimate strength f_{tu}	140 MPa / 0.1* MPa
Plastic tensile strain at peak ε_{tp}^p	0.55%
Fracture energy in tension $G_{f,t}$	2.56* kNm/m^3
Compressive yield strength f_{cy}	160 MPa
Compressive peak strength f_{cp}	560 MPa
Compressive ultimate strength f_{cu}	560 MPa
Plastic compressive strain at peak ε_{cp}^p	0.55%
Parameter hardening curve tension K_t	10^6 MPa
Parameter hardening curve tension c$_t$	1.0
Parameter hardening curve compression K_c	10^6 MPa
Parameter hardening curve compression c$_c$	1.0

* only applicable to the analyses using strain-softening.

assumption of full overburden acting on the tunnel lining does not necessarily hold true in practice and so the applied stresses might be associated with different tunnel depths to those considered here. Lastly, the bending moment at the joint was imposed via a vertical load acting along the width of the segment at about 0.5 m from the joint. A downward load was applied in the analyses where positive bending (i.e. opening at the intrados) was considered whereas an upward load was applied in those where negative bending (i.e. opening at the extrados) was examined. Since the magnitude of the vertical load required for the joint to reach its ultimate capacity was unknown beforehand, it was gradually increased throughout the analysis and a maximum number of iterations set for terminating the analysis which ensured that the M-θ curve derived from every analysis had reached a plateau.

The elasto-plastic model for GCI introduced by Ruiz López et al. (2022a) was employed to simulate the constitutive behaviour of the segment flanges and skin. The same material calibration employed by Ruiz López et al. (2022a) was adopted in the analyses presented here. The model parameters are presented in Table 1. As the base condition of the investigation, material failure was represented as material hardening reaching a plateau such that the peak strength was set equal to the ultimate strength ($f_{tp} = f_{tu}$ and $f_{cp} = f_{cu}$). Nevertheless, strain-softening was incorporated in several analyses in order to simulate the potential tensile fracturing of GCI. It is well known that FE solutions become sensitive to the mesh discretization when strain-softening is adopted. This issue can be alleviated with regularisation methods, which in some way or other introduce a characteristic length into the formulation. The fracture energy approach (Hillerborg et al., 1976), also known as crack band model, is one of such regularisation methods essentially based on adjusting the softening rate according to the element size. The fracture energy G_f can be defined as the amount of energy dissipated by the material per unit of fracture surface area. The objectivity of the FE solution is satisfied with the fracture energy approach by enforcing the following expression:

$$G_f = g_c \cdot l_c \tag{1}$$

where g_c is the area underneath the stress-(plastic) strain softening curve and l_c is the element characteristic length, defined in the elasto-plastic

model as $l_c = \sqrt[3]{V_e/n_{ip}}$, where V_e is the volume of the element and n_{ip} is the number of integration points of the element (Schütz, 2010). The fracture energy G_f is related to the fracture toughness K_{Ic} with the relationship (Irwin, 1957):

$$G_f = \frac{K_{Ic}^2}{E} \tag{2}$$

where E is the elastic modulus. The fracture toughness K_{Ic} was adopted as 16 MPa.m$^{1/2}$ in this study which corresponds to the lower bound (on the brittle side) of the measurements established for GCIs with a tensile strength of around 140 MPa as gathered by Bradley & Srinivasan (1990). According to Expression (2), the fracture energy value in tension $G_{f,t}$ was adopted in the analyses employing strain-softening as 2.56 kNm/m^2. Finally, the ultimate tensile strength f_{tu} was set to a residual value of 0.1 MPa.

The material modelling of the interface elements and bolting system followed from Ruiz López et al. (2022a). The linear elastic perfectly-plastic Mohr-Coulomb criterion was employed for the interface elements. The normal and shear stiffness were adopted as 10^{10} kN/m^3 while the angle of shearing resistance was taken as 40°. The elastic perfectly-plastic von Mises model was employed for the bolting system. The value of the bolting stiffness was adopted as 50 GPa and the yield strength as 239 MPa.

4. Analysis cases

Table 2 presents a summary of the analyses conducted in this investigation. The characterisation of the joint behaviour of the 11 ft 8$^{1/4}$ in and the 21 ft 2$^{1/2}$ in tunnel geometries (IDs 1 and 2 in Table 2) involved analyses under positive and negative bending where the joint was subjected to four different axial compression levels; the analyses under positive bending were conducted adopting strain-softening and without it, so that a total of twelve analyses was performed for each joint geometry. Additional analyses were conducted to assess the impact on the joint response of several factors. First, the impact of removing the bolts from the joint prior to the start of the analyses was considered (ID 3), this is relevant because while it is commonly assumed that undoing the bolts of certain tunnel sections enables the changes in tunnel lining stresses to be minimised when an existing tunnel is subjected to new solicitations, the effect of doing so has not been evaluated in comparison with the response of a bolted joint. Again, analyses under positive and negative bending subjected to the four compression levels were considered. Secondly, the impact of the bolt preload magnitude was investigated (ID 4) comparing the behaviour of the joint with bolt preloads corresponding to 12.5%, 25% (base condition) and 50% of the tensile force at yield. These were assessed for a tunnel depth of 12 m under positive and negative bending. Lastly, the influence of the out-of-plane restraint condition applied on the circumferential flanges was investigated (ID 5). The base restraint condition (i.e. displacements fixed along the full height of the flange) was compared to restraining only the upper part (up to the thickness of the skin) of the circumferential flange. This comparison was carried out for analyses adopting a tunnel depth of 12 m under positive and negative bending.
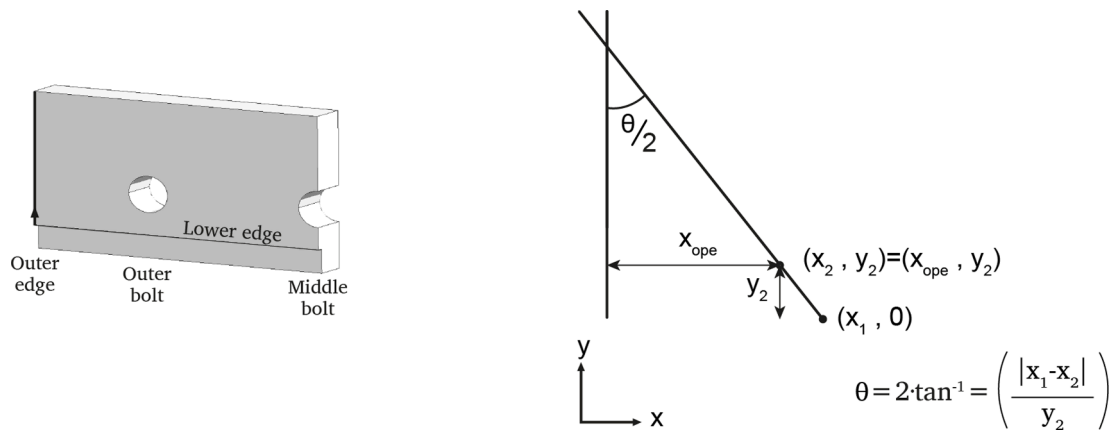
Table 2
Summary of analyses conducted in the numerical investigation.

ID	Tunnel geometry	Bolted/non-bolted	Tunnel depth (m)	Bending mode	Strain-softening	Sensitivity study
1	11 ft 8$^{1/4}$ in	Bolted	6, 12, 24, 48	Pos./neg.	Yes (pos.)	–
2	21 ft 2$^{1/2}$ in	Bolted	6, 12, 24, 48	Pos./neg.	Yes (pos.)	–
3	11 ft 8$^{1/4}$ in	Non-bolted	6, 12, 24, 48	Pos./neg.	No	Removal of the bolts
4	11 ft 8$^{1/4}$ in	Bolted	12	Pos./neg.	No	Bolt preload
5	11 ft 8$^{1/4}$ in	Bolted	12	Pos./neg.	No	Out-of-plane restraint

Fig. 4. Definition of joint rotation as employed in the numerical investigation.

$$\theta = 2 \cdot \tan^{-1} = \left(\frac{|x_1 - x_2|}{y_2} \right)$$

(a) Positive bending (faint curves are from analyses without strain softening)

(a) Negative bending

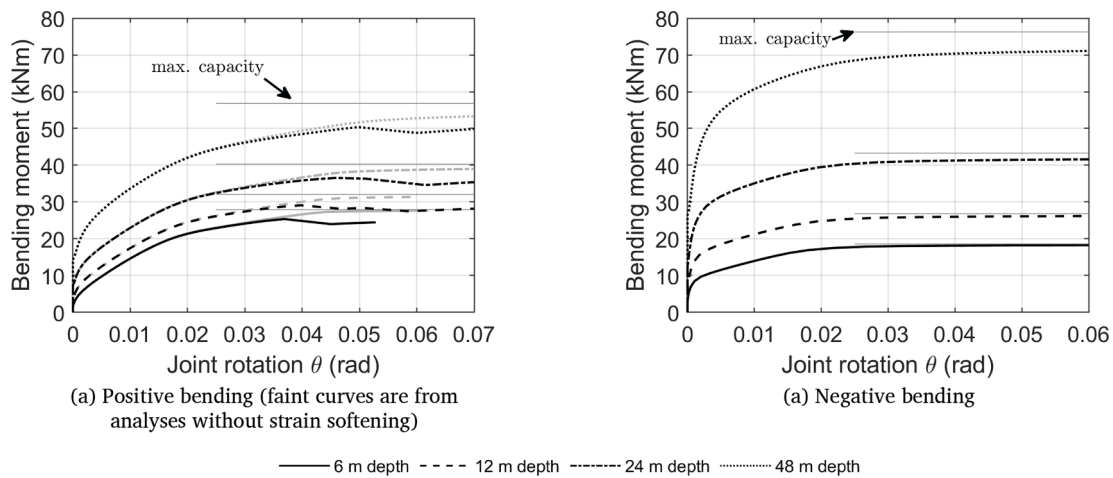——— 6 m depth - - - - 12 m depth ------- 24 m depth ·········· 48 m depth

Fig. 5. Bending moment (kNm) with joint rotation (rad) under different overburden pressures – 11 ft $8^{1/4}$ in (3.562 m) running tunnel geometry.

5. Definition of joint rotation

It has been shown experimentally (Afshan et al., 2017) and numerically (Ruiz López, 2022) that the GCI tunnel joint does not rotate uniformly when subjected to positive bending. This is a consequence of tension being generated only along the width of the circumferential flange such that the rotation is maximum at the outer edge of the joint and gradually reducing towards the middle location of the joint. It was decided to adopt the joint rotation as that occurring at the outer edge of the joint as representative of the rotation over the entire joint. This was motivated by the fact that this location is effective in transferring stress between the circumferential and longitudinal flanges, whereas the rest of the longitudinal flange is mechanically active only through the action of the bolts. The validity of adopting the rotation at the outer edge is demonstrated in a separate paper by Ruiz López et al. (2022b) where a newly developed joint model was calibrated against the M-θ curves derived here and subsequently utilised in a series of structural analyses on a segmental GCI ring with beam elements. The predicted stiffness degradation at the joints and globally around the ring were in excellent agreement with analogous 3D analyses, which indicates that the rotational stiffness of the joint is represented well.

The results of the 3D FE analyses were interpreted by considering that joint rotation only occurs once the joint first opens. Moreover, the rotation was calculated as $\theta = 2 \cdot \tan^{-1}(|x_1 - x_2|/y_2)$ where x_1 is the opening of the node located at the lower edge of the joint in positive bending (and the extrados in negative bending), x_2 is the opening of the node closest to the previous one along the height of the joint, and y_2 is

the distance from the edge of the joint (lower edge in positive bending or the extrados in negative bending) to that node. Fig. 4 illustrates the approach for calculating the rotation. As shown in Appendix A, such an approach proved to give the best overall match, compared to other procedures, with the numerical data in most of the portion of the cross-section experiencing opening.

6. Numerical characterisation of the rotational response

6.1. 11 ft $8^{1/4}$ in (3.562 m) running tunnel

6.1.1. M-θ response and behaviour of the bolts

Fig. 5 depicts the M-θ curves for positive and negative bending modes obtained with the 11 ft $8^{1/4}$ in tunnel joint geometry. The rotational stiffness (i.e. tangent of the M-θ curves) gradually reduces from its initial magnitude immediately after opening until the M-θ curves reach a plateau meaning the ultimate bending moment has been attained. As expected, the bending moment of opening and ultimate bending moment both increase with tunnel depth. The joint response is significantly different under positive and negative bending. First, larger bending moments of opening are predicted, for a given tunnel depth, under negative bending. The bending moment of opening is that at which the compression stress at the edge of the joint becomes zero, consequently, the observed differences between the two bending modes can be explained by the U cross-section of the GCI segment: as the centroid of the segment is closer to the extrados than the intrados, the section modulus Z ($Z = I/y$, where I is the second moment of area and y
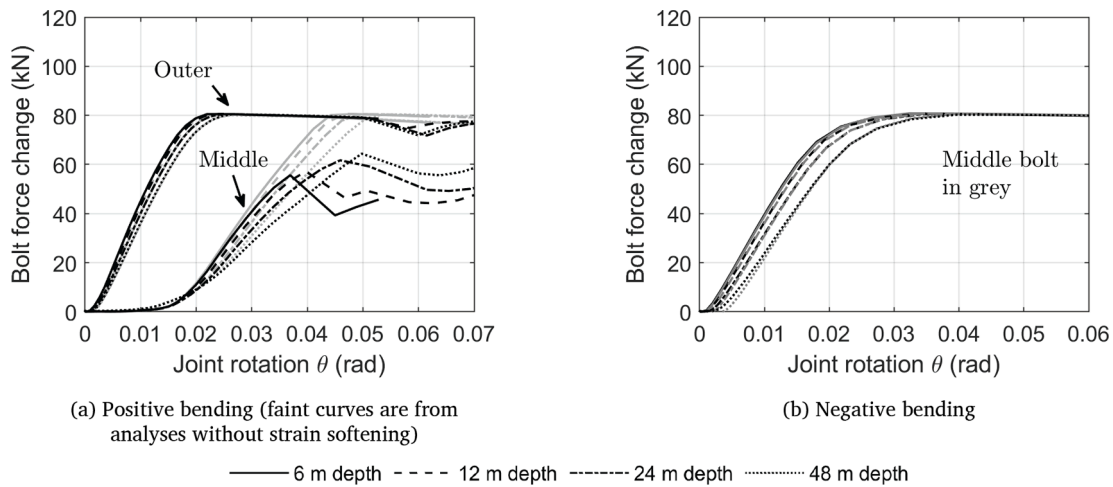
Fig. 6. Change in bolt force (kN) with joint rotation (rad) under different overburden pressures – 11 ft 8$^{1/4}$ in (3.562 m) running tunnel geometry.

is the distance from the extreme fibre to the centroid) is larger for the former and so the joint reaches tension at smaller bending moments at the intrados (positive bending) than at the extrados (negative bending). A distinct response is also observed with respect to the ultimate bending moments. Fig. 5 indicates that the ultimate bending moment is larger under positive bending for 6 m and 12 m tunnel depths whereas it is larger under negative bending for tunnel depths of 24 m and 48 m. These differences relate to the distinct contribution of the bolts and axial force to the ultimate bending moment: the former is larger under positive bending whereas the contribution from the axial force is larger under negative bending. Furthermore, the M-θ curves corresponding to the analyses adopting strain-softening under positive bending (darker lines in Fig. 5) soften slightly near the end of the curves and somewhat stabilise at a constant value subsequently. As shown later, this is related to a reduction in bolt forces, in turn caused by the strain-softening experienced by the flange. The effect of considering strain-softening is only clearly reflected on the M-θ curves after a large joint rotation (around 0.035 rad) as can be observed through comparison with the M-θ curves generated from the analyses without strain-softening (faint lines).

Fig. 6 presents the change in bolt force, from the initial preload, with joint rotation. Under positive bending (Fig. 6a), the outer bolts sustain nearly all tensile loading until they yield and the middle bolt sustains all subsequent tension. The outer bolts initially taking a greater fraction of the tensile loading has been observed experimentally (Thomas, 1977, Afshan et al., 2017) and can be attributed to tension, under positive bending, being initiated at the intrados of the circumferential flanges and hence, more easily transferred to the outer bolts. It can be observed that the outer bolts reach their ultimate load in all analyses with strain-softening following the same loading path up to yielding as in the analyses without strain-softening (faint line). On the other hand, when strain-softening is considered, the middle bolt does not mobilise its full tensile strength due to the softening taking place around the longitudinal flange. The middle bolt experiences a force reduction when the change in bolt force is around 60 kN (corresponding, in absolute terms, to about 80% of its tensile strength) with all tunnel depths. It can be observed that the softening of the middle bolt occurs earlier (i.e. at smaller rotations) and is more abrupt for smaller tunnel depths. The unloading of the middle bolt is followed by the force increasing slightly and finally levelling out. The outer bolts also experience unloading from a joint rotation of about 0.05 rad although such unloading is less pronounced than that of the middle bolt and is recovered subsequently.

Under negative bending (Fig. 6b), tension develops uniformly along the extrados of the skin under negative bending and accordingly, the bolt forces develop simultaneously with rotation. The distinct response of the bolts under both bending modes was first observed in the numerical analyses conducted by Tsiampousi et al. (2017).

The M-θ response of the joint is largely governed by the behaviour of the bolts and obvious correlations between the two can be established. Under positive bending, there is a slight reduction in the slope of the M-θ curves around a joint rotation of 0.02 rad which is explained by yielding of the outer bolts. Similarly, the M-θ curves under negative bending (nearly) reach their plateau between 0.02 and 0.035 rad which is the rotation range over which the bolt forces yield in those analyses.

6.1.2. Tensile behaviour of the segments

Fig. 7 depicts contour plots of the tension hardening variable of the elasto-plastic model used for GCI, $\tilde{\varepsilon}_1^p = \int d\varepsilon_1^p$, at different rotation levels from the analysis under positive bending corresponding to a tunnel depth of 12 m. Three views are included for each rotation level: inside of the segment and longitudinal flange (top), outside of the segment having removed (for visual inspection) the elements representing the longitudinal flange (middle) and outside of the longitudinal flange. Contours in light red indicate tensile strains between 0 and 0.55%, which is the magnitude of the plastic strain at peak tensile strength ε_{tp}^p (see Table 1), and contours in darker red show tensile strains larger than 0.55% i.e., the areas coloured in darker red are undergoing softening. There are two zones where softening occurs, see top Fig. 7a: zone 1, along the height of the circumferential flange adjacent to the longitudinal flange; and zone 2, along the width of the internal side of the skin also adjacent to the longitudinal flange. It is worth noting that zone 1 is the location where the segment fractured in one of the structural tests conducted by Afshan et al. (2017) on a half-scale GCI ring at Imperial College London, which is an indication that the numerical model is able to reproduce, at least to some extent, the mode of potential tensile failure of the joint.

At a rotation of 0.031 rad (Fig. 7a), significant strain localisation has already developed in zone 1 whereas zone 2 is still relatively thin and confined to the bottom of the skin. At larger rotations (Fig. 7b-d), the height of zone 1 remains nearly constant and so does its width across the circumferential flange, whereas it propagates across the longitudinal flange (see top view). Zone 2 propagates extensively across the width of the skin, particularly towards the middle of the segment between rotations of 0.031 rad and 0.046 rad. Such propagation enables the middle part of the longitudinal flange to deform somewhat independently from the rest of the segment, causing a reduction of the joint opening at the middle location and the consequent unloading of the middle bolt observed in Fig. 6a. By a joint rotation of 0.058 rad (Fig. 7d) softening develops at two locations around the outer bolts holes propagating diagonally across the contact surface of the longitudinal flange and across most of the longitudinal flange thickness. The failure occurring around the bolt holes is responsible for the unloading observed in the outer bolts forces between 0.05 and 0.058 rad. Clearly, extensive areas
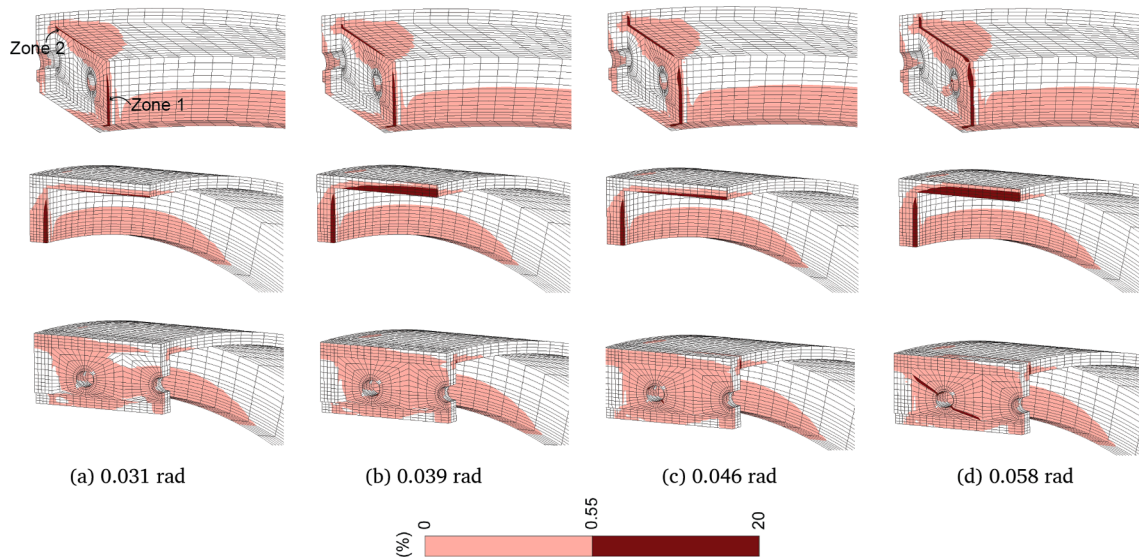
(a) 0.031 rad   (b) 0.039 rad   (c) 0.046 rad   (d) 0.058 rad

Fig. 7. Contour plots of the tension hardening variable $\tilde{\varepsilon}_1^p$ of the elasto-plastic model adopted for GCI at various rotation levels for the analysis under positive bending (with strain-softening) on the 11 ft $8^{1/4}$ in (3.562 m) running tunnel geometry for a 12 m tunnel depth.

of the joint have experienced strain-softening by the end of the analyses and yet complete breakage of the joint is not realised and the bolt forces do not fully soften. Accordingly, the ultimate bending moments are not too dissimilar from those attained in the analyses without strain-softening. It is worth pointing out that in the laboratory test performed by Afshan et al. (2017), the segment fractured across the circumferential flange which is unlike the numerical analyses described here, where zone 1 propagates towards the longitudinal flange and not completely through it. This could be related to differences in the boundary conditions (in the laboratory, the axial force acting on the joint was not constant and one of the circumferential flanges was free to deform in the out-of-plane direction), the effects of a loading–unloading cycle applied in the laboratory test and not considered here, size effects (the laboratory test was performed on a half-scale prototype) and to simplifications in the geometry of the numerical model, e.g. neglecting the presence of the fillet radiuses between the longitudinal and

circumferential flanges and between the skin and the longitudinal flange.

6.1.3. Compressive behaviour of the segments

Reverting back to the M-θ curves, it is useful to compare their ultimate bending moments with the maximum joint capacity, depicted with the grey horizontal lines in Fig. 5. This is introduced here as the ultimate bending moment determined with the assumptions that the bolts reach their ultimate tensile strength and that the segments remain elastic, implying that the contact force between segments is shifted all the way to the edge of the joint. Fig. 8 depicts the stress state assumed in the calculation of the maximum capacity. Under positive bending, the maximum capacity is calculated with the following expression:

$$M^{max} = N \cdot y_o + [(h - h_{G1}) + 2(h - h_{G2})]A_b \cdot f_{tu,b} \tag{3}$$

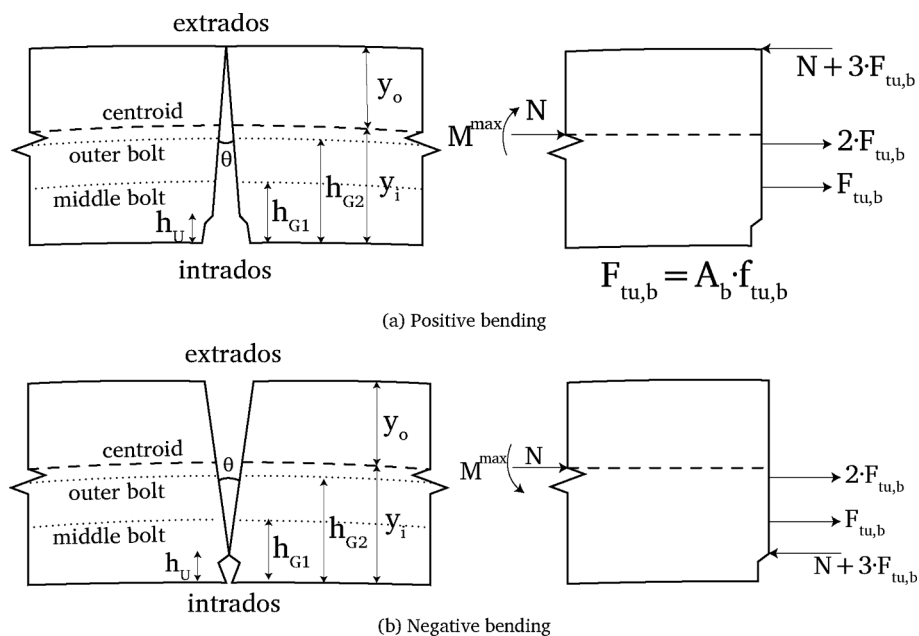where N is the (circumferential) axial force, y_o is the distance from the

(a) Positive bending

(b) Negative bending

Fig. 8. Stress state assumed in the maximum capacity calculation.

(a) 6 m depth

(b) 12 m depth

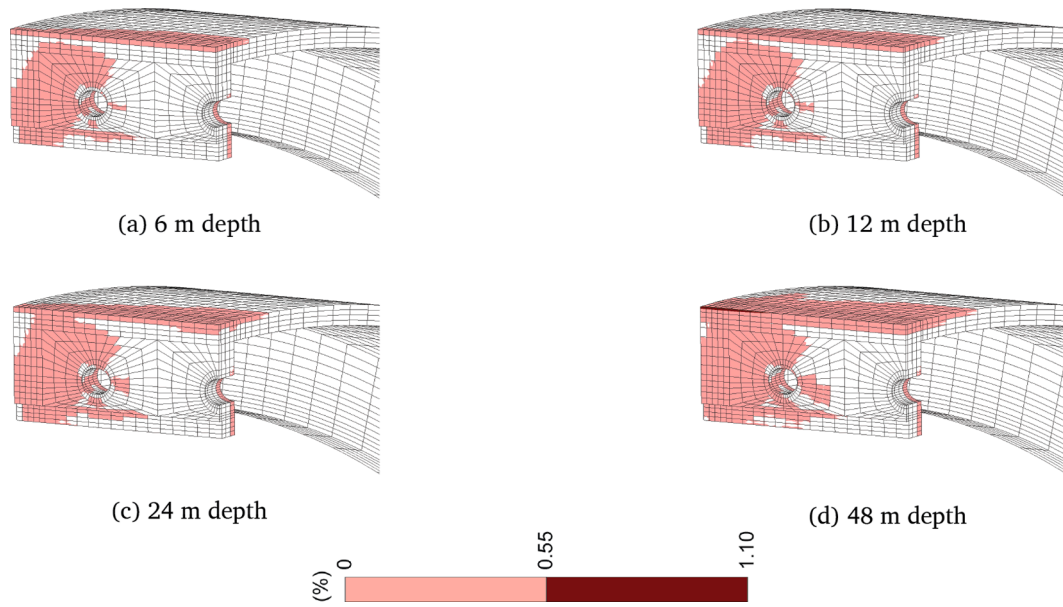(c) 24 m depth

(d) 48 m depth

Fig. 9. Contour plot distribution of the compression variable parameter $\widetilde{\varepsilon}_3^p$ of the elasto-plastic model employed for GCI at the end of the analyses (without strain-softening) under positive bending – 11 ft $8^{1/4}$ in (3.562 m) running tunnel geometry.

extrados to the centroid of the segment, h is the height of the segment, h_{G1} and h_{G2} are the distances from the intrados to the middle bolt and the outer bolts centrelines, A_b is the bolt thread cross-section area and $f_{tu,b}$ is the uniaxial tensile strength of the bolts. For negative bending, the maximum capacity is:

$$M^{max} = N \cdot (y_i - h_U) + [(h_{G1} - h_U) + 2(h_{G2} - h_U)]A_b \cdot f_{tu,b} \qquad (4)$$

where y_i is the distance from the intrados to the centroid of the segment and h_U is the depth of the caulking groove. Note that the axial force N obtained in the analyses corresponds to 118 kN, 236 kN, 472 kN and 944 kN for tunnel depths of 6 m, 12 m, 24 m and 48 m, respectively.

In the case of the analyses under positive bending and adopting strain-softening, the differences between the ultimate bending moments and the maximum capacity obtained in the analyses mostly reflect the impact of the middle bolt not reaching its tensile strength. For tunnel depths of 6–24 m, the ultimate bending moments given by the analyses under positive bending without strain-softening are only slightly smaller than the maximum capacity and the same applies for the analyses under negative bending (Fig. 5b). More significant differences are however observed in the ultimate bending moments obtained for a tunnel depth of 48 m. Some differences with respect to the maximum capacity could be expected because the maximum capacity calculation considers that the compressive force is acting at the edge of the joint along an infinitely thin area while in the numerical model the force is distributed over a finite area and so the lever arm is necessarily smaller. Additionally, the gradual reduction of the surface area under compression that takes place with rotation can eventually result in compressive failure of the contact zone.

In this respect, Fig. 9 and Fig. 10 show contour plots of the compression hardening variable, $\widetilde{\varepsilon}_3^p = \int d\varepsilon_3^p$, of the constitutive model adopted for GCI, corresponding to the end of the analyses for positive (without strain-softening) and negative bending, respectively. Plastic strains of magnitude greater than the compressive plastic strain at peak $\varepsilon_{cp}^p = 0.55\%$ indicate that the material has exhausted its strength at those points. Under positive bending (Fig. 9), the largest compressive strains take place along the width of the segment near the extrados. Compressive failure only occurs in some of the integration points that are closest to the extrados in the analysis for a tunnel depth of 48 m.

Under negative bending (Fig. 10), the compression stresses transfer mainly along the circumferential flanges and so the maximum

compressive strains locate near the outer edge of the joint, just above the caulking groove. The compressive strains exceed ε_{cp}^p in several integration points in all the analyses with the surface area undergoing failure increasing with the tunnel depth. Even though the material reaches compressive failure close to the edges of the joint, the entire portion of the joint under compression does not fail in any of the analyses under positive or negative bending. The contact zone is not failing in compression because it does not become sufficiently small for this to happen for the compression levels considered in this investigation.

Fig. 11 presents the variation of the joint height under compression with rotation for different tunnel depths under positive and negative bending. The height subjected to compression was determined at the outer edge of the joint to be consistent with the definition of rotation, as explained in Section 5. It can be observed that the height subjected to compression decreases rapidly as the joint starts rotating and more gently subsequently. The rate at which that occurs is slower for deeper tunnels and for the analyses under negative bending. By the end of the analyses, the height under compression is less than 1 cm for most cases and it is still reducing, particularly in the analyses under negative bending.

6.2. 21 ft $2^{1/2}$ in (6.464 m) station tunnel geometry

The results obtained with the 21 ft $2^{1/2}$ in tunnel joint geometry are presented in this section. As discussed in Section 2, the middle bolt in this geometry is offset, towards the intrados, with respect to the outer bolts which leads to a distinct bolt action with respect to that discussed in Section 6.1 for the 11 ft $8^{1/4}$ in tunnel geometry. Additionally, the magnitudes of the bending moments (and axial forces acting at the joint) are considerably larger than those observed in the 11 ft $8^{1/4}$ in tunnel geometry due to the greater dimensions of the tunnel geometry.

6.2.1. M-θ response and behaviour of the bolts

Fig. 12 presents the M-θ curves for the 21 ft $2^{1/2}$ in tunnel joint geometry under positive and negative bending, note that the axial force N used in the maximum capacity calculations, Expressions (3) and (4), corresponds to 193 kN, 386 kN, 772 kN and 1544 kN for tunnel depths of 6 m, 12 m, 24 m and 48 m, respectively. The magnitudes of the bending moments of opening and ultimate bending moments follow the same hierarchy between positive and negative bending as the 11 ft $8^{1/4}$ in
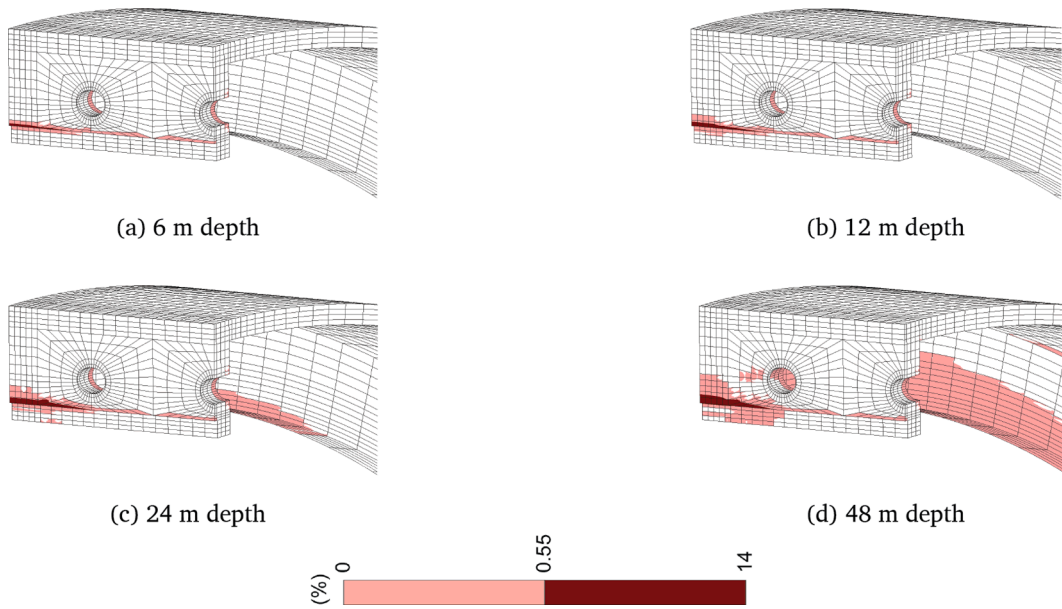
(a) 6 m depth

(b) 12 m depth

(c) 24 m depth

(d) 48 m depth

Fig. 10. Contour plot distribution of compression hardening variable $\tilde{\varepsilon}_3^p$ of the elasto-plastic model employed for GCI under negative bending – 11 ft $8^{1/4}$ in (3.562 m) running tunnel geometry.
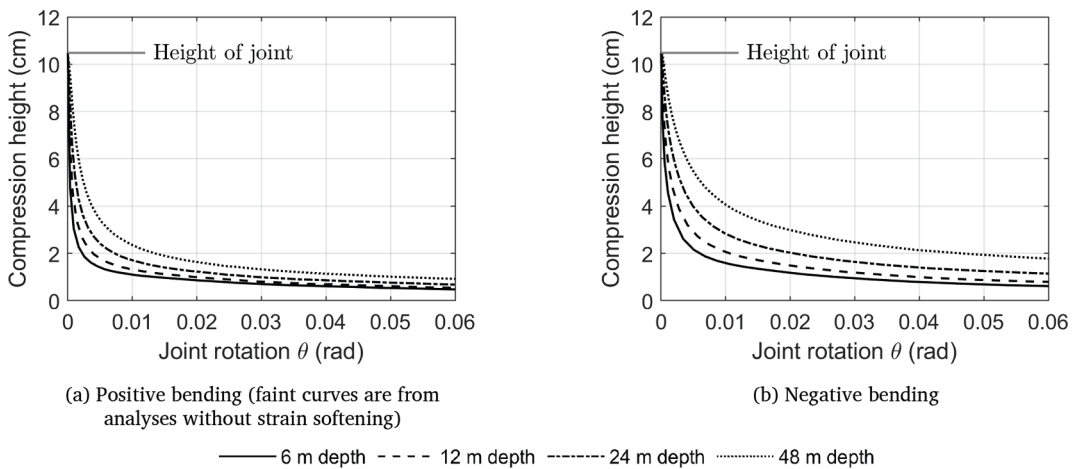

(a) Positive bending (faint curves are from analyses without strain softening)

(b) Negative bending

—— 6 m depth   - - - - 12 m depth   -------- 24 m depth   ·········· 48 m depth

Fig. 11. Height under compression (cm) with joint rotation (rad) under different overburden pressures – 11 ft $8^{1/4}$ in (3.562 m) running tunnel geometry.
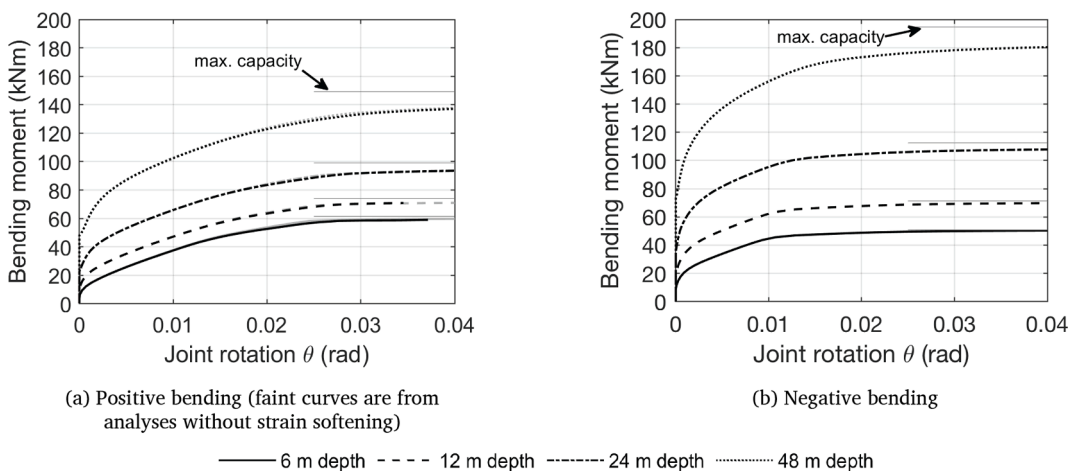

(a) Positive bending (faint curves are from analyses without strain softening)

(b) Negative bending

—— 6 m depth   - - - - 12 m depth   -------- 24 m depth   ·········· 48 m depth

Fig. 12. Bending moment (kNm) with joint rotation (rad) under different overburden pressures – 21 ft $2^{1/2}$ in (6.464 m) station tunnel geometry.
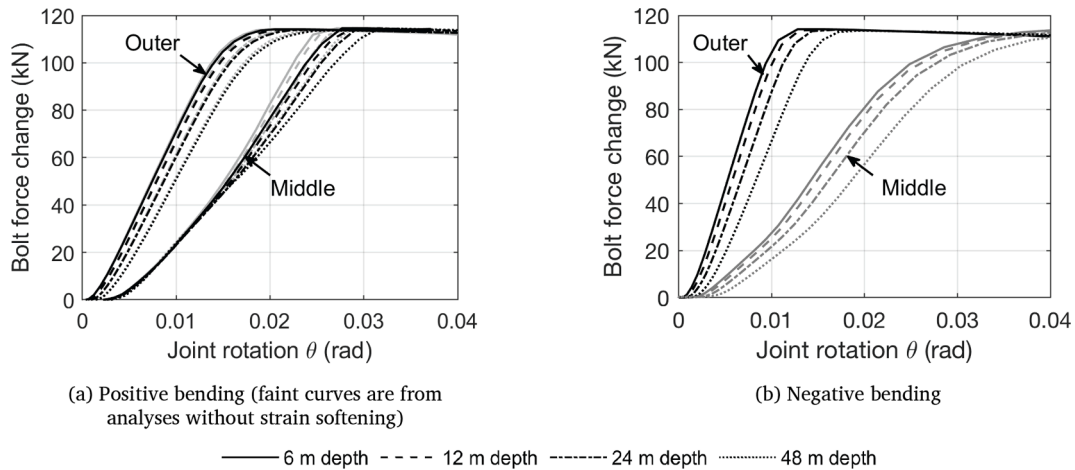
(a) Positive bending (faint curves are from analyses without strain softening)

(b) Negative bending

―――― 6 m depth　- - - - 12 m depth　-------- 24 m depth　·········· 48 m depth

Fig. 13. Change in bolt force (kN) with joint rotation (rad) under different overburden pressures – 21 ft $2^{1/2}$ in (6.464 m) station tunnel geometry.
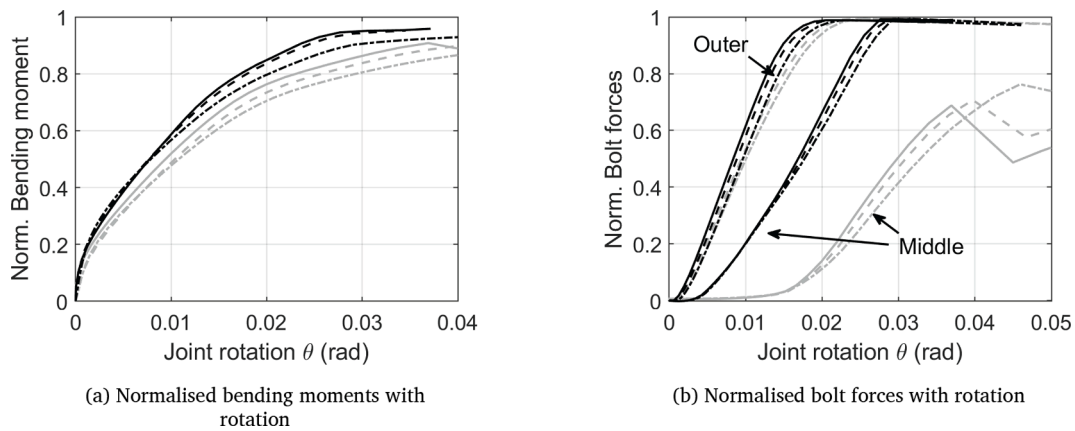

(a) Normalised bending moments with rotation

(b) Normalised bolt forces with rotation

Fig. 14. Normalised joint response of the 21 ft $2^{1/2}$ in (6.464 m) station tunnel geometry and the 11 ft $8^{1/4}$ in (3.562 m) running tunnel geometry (faint curves) under positive bending.

tunnel geometry (Fig. 5) for the same reasons outlined in Section 6.1. The M-θ curves corresponding to the analyses considering strain-softening are virtually indistinguishable from those obtained in the analyses without strain-softening (shown with a faint line). This is despite tensile failure occurring around the longitudinal flange, as explained in Section 6.2.2. Fig. 13 depicts the change in bolt force with rotation. First, negligible differences between the analyses with and without strain-softening, under positive bending, can be observed in the loading path followed by the outer bolts whereas minor ones can be found in the response of the middle bolt: the analysis considering strain-softening exhibits a slightly softer response from a rotation of around 0.015 rad. It can also be observed that the outer and middle bolts develop tensile forces from early rotation levels under positive bending (Fig. 13a) and even though the middle bolt force increases at a slower rate, the tensile forces are more evenly distributed between the outer and middle bolts than they were in the 11 ft $8^{1/4}$ in tunnel geometry, where the middle bolt developed negligible tension prior to yielding of the outer bolts. Regarding the bolts' response under negative bending (Fig. 13b), the force of the middle bolt develops at a slower rate than that of the outer bolts which again can be attributed to the middle bolt being offset from the outer bolts, since the joint opens at the extrados and rotates uniformly along its width, the middle bolt sustains less elongation than the outer bolts for a given rotation. It is worth noting that the contribution of the middle bolt to the joint capacity under negative bending is largely negligible due to the small lever arm to the lower edge of the joint, this can be observed in that the M-θ curves nearly reach their plateau after the yielding of the outer bolts and prior to the complete development of

the middle bolt force. The behaviour of the 21 ft $2^{1/2}$ in tunnel joint is particularly different from that of the 11 ft $8^{1/4}$ in tunnel joint under positive bending. These differences are explored in Fig. 14 where the normalised bending moments with rotation and the normalised change in bolt forces with rotation are plotted for the analyses under positive bending (considering strain-softening) with tunnel depths of 6–24 m. The normalised bending moments were obtained as $(M - M_o)/(M^{max} - M_o)$ where M is the bending moment and M_o corresponds to the bending moment attained in the last analysis increment prior to joint opening; the normalised bolt forces were calculated as $(F_b - F_{bo})/(F_{bu} - F_{bo})$ where F_b is the bolt force, F_{bo} is the bolt preload and F_{bu} is the ultimate bolt force. The normalised bending moments (Fig. 14a) from the 21 ft $2^{1/2}$ in tunnel joint converge more rapidly towards the plateau than the corresponding curves from the 11 ft $8^{1/4}$ in geometry. As shown in Fig. 14b, the outer bolts forces increase at similar rates with rotation in the two geometries whereas the middle bolt starts developing force significantly earlier and at a higher rate in the 21 ft $2^{1/2}$ in tunnel joint. The earlier development of tension, and consequent yielding, of the middle bolt is the primary reason for the M-θ curves reaching their plateau at lower rotations than they do in the 11 ft $8^{1/4}$ in geometry.

6.2.2. Tensile behaviour of the segments

The potential for tensile failure of the GCI segments is considered here for the analyses under positive bending considering strain-softening. Fig. 15 depicts contour plots of the tension hardening variable $\tilde{\varepsilon}_1^p$ of the elasto-plastic model used for GCI at various joint rotation levels for a tunnel depth of 12 m. As with the 11 ft $8^{1/4}$ in geometry, the
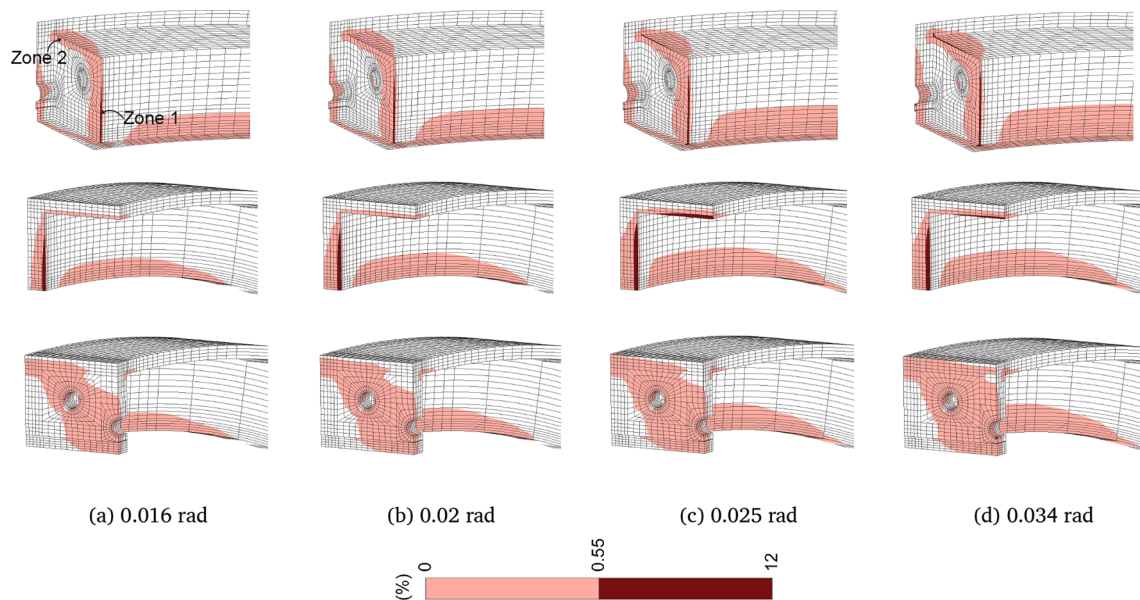
| (a) 0.016 rad | (b) 0.02 rad | (c) 0.025 rad | (d) 0.034 rad |

Fig. 15. Contour plots of tension hardening variable $\widetilde{\varepsilon}_1^p$ at various rotation levels for the analysis under positive bending (with strain-softening) on the 21 ft $2^{1/2}$ in (6.464 m) station tunnel geometry for a 12 m tunnel depth.

maximum tensile strains are located along the circumferential flange adjacent to the longitudinal flange (zone 1) and along the internal side of the skin adjacent to the longitudinal flange (zone 2). It can be observed that while zone 2 develops towards the extrados throughout the analysis, it propagates less prominently, relative to the cross-section, than in the 11 ft $8^{1/4}$ in geometry (bottom plots of Fig. 7). The width of zone 1 across the circumferential flange remains nearly constant throughout the analysis whereas it develops towards the longitudinal flange as occurred in the 11 ft $8^{1/4}$ in geometry, albeit to a lesser degree. Overall, the numerical results indicate that the extent of tensile failure of the segment is far less significant than that observed in the running tunnel geometry. This is consistent with Fig. 12a which shows that the impact of considering strain-softening on the M-θ curves is negligible, as opposed to its greater significance in the 11 ft $8^{1/4}$ in M-θ response, as observed in Fig. 5.

6.2.3. Compressive behaviour of the segments

Fig. 16 presents contour plots of the compression hardening variable $\widetilde{\varepsilon}_3^p$ of the constitutive model used for GCI at the end of the analyses, under positive and negative bending, corresponding to 48 m tunnel depth. These are the analyses subjected to larger compression and so exhibit the largest compressive strains. Under positive bending

(Fig. 16a), compressive plastic strains take place along the width of the skin close the extrados. Plastic strains also develop on the contact face of the joint around the outer bolts as well as around the bolt holes on the internal face of the flange. The latter is the result of the action of the bolt nut on the flange. The magnitude of the compressive plastic strains is below the compressive plastic strain $\varepsilon_{cp}^p = 0.55\%$ and so failure in compression does not occur under positive bending. Under negative bending (Fig. 16b), compressive plastic strains occur at the lower edge of the joint, particularly towards the outer edge where most of the compression is transferred across the segments. There is a relatively thin area where strains surpass the value of $\varepsilon_{cp}^p = 0.55\%$ (darker contour), however, the size of this area is less than the portion of the joint under compression so that complete failure in compression is not attained.

In summary, the numerical investigation on the longitudinal joint of the 21 ft $2^{1/2}$ in station tunnel revealed several differences in behaviour compared to the running tunnel joint that had not been previously observed. Under positive bending, the middle bolt is mobilised from small rotations leading to the joint reaching the end of its capacity earlier than in the running tunnel geometry. The size of the region affected by tensile failure is smaller, relatively speaking, than that observed in the running tunnel geometry and the effects of tensile failure on the joint behaviour are negligible as compared to the other geometry.
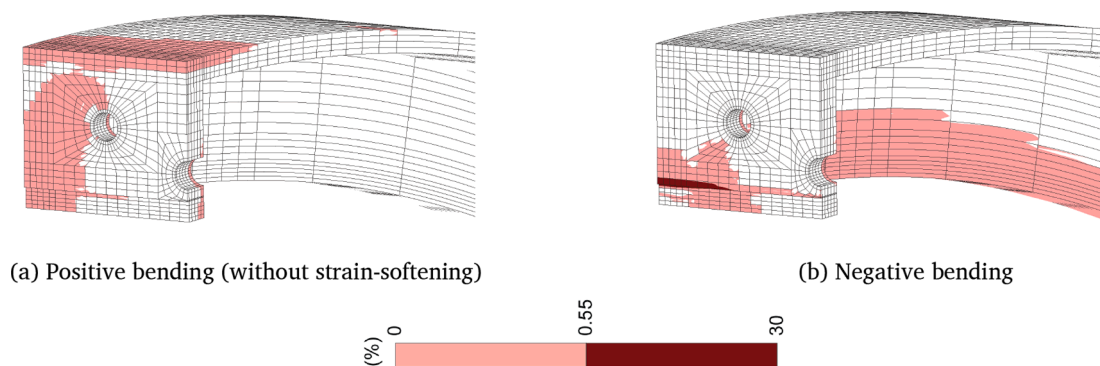

| (a) Positive bending (without strain-softening) | (b) Negative bending |

Fig. 16. Contour plot distribution of the compressive plastic strain ε_3^p at the end of the analyses under positive bending – 21 ft $2^{1/2}$ in (6.464 m) station tunnel geometry.
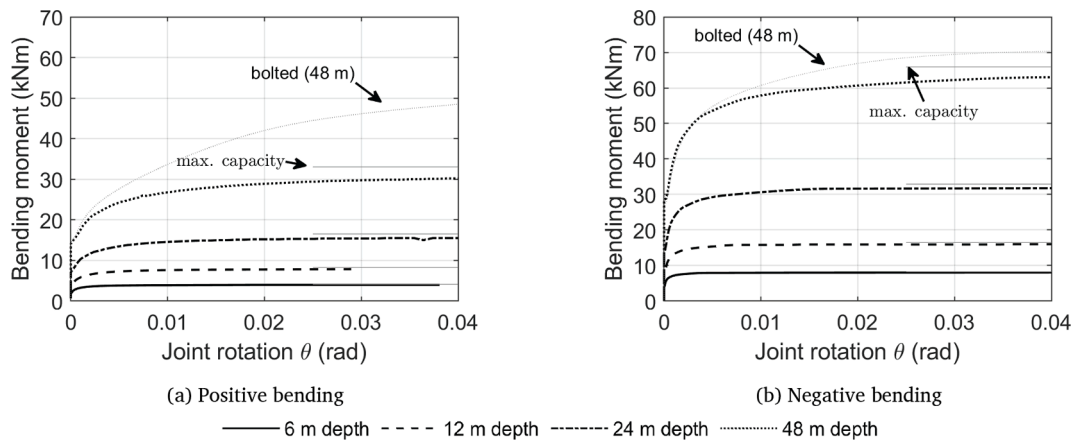
Fig. 17. Bending moment (kNm) with joint rotation (rad) under different overburden pressures – 11 ft 8$^{1/4}$ in (3.562 m) running tunnel geometry without bolts.

Under negative bending, the contribution of the middle bolt to the joint stiffness and capacity is negligible compared to that observed in the running tunnel geometry where the three bolts behaved equally.

7. Factors affecting the rotational behaviour of tunnel joints

The following analyses were conducted for the 11 ft 8$^{1/4}$ in geometry. As they did not consider strain-softening, they were carried out adopting the FE mesh presented in Fig. B1b to decrease their computational cost. Appendix B discusses the mesh dependency of the results, which was negligible.

7.1. Effect of removing the bolts

The analyses presented in this section followed the analysis procedures outlined in Section 3 except for the presence of the bolts which were removed from the mesh before the analyses started.

Fig. 17 depicts the M-θ curves obtained under positive and negative bending along with the maximum capacity corresponding to each tunnel depth as given by Equations (3) and (4). To facilitate the discussion, the M-θ curves obtained in the analyses with bolts (shown in Section 6.1) for a tunnel depth of 48 m are also included in Fig. 17. The early parts of the M-θ curves with and without bolts are very similar, which indicates that the presence of the bolts has negligible impact on the bending moment at which the joint opens and on the initial rotational stiffness immediately after opening. This is reasonable because, as shown in Fig. 6, the bolts are mobilised only after certain joint rotation has taken place. As expected, the ultimate bending moments are smaller than those obtained with bolts. More significant differences can be observed under positive bending because, as already demonstrated, the contribution of the bolts is greater under this mode. The magnitudes of the ultimate bending moments obtained in the analyses without bolts are generally very close to the corresponding maximum capacity, particularly for the analyses with smaller tunnel depths in which the area of the joint under compression reduces more rapidly with rotation. Furthermore, the ultimate bending moments are attained at significantly smaller rotations when the bolts are removed: without the bolts, the M-θ curves for tunnel depths of 6–24 m have largely reached their plateau when the joint rotates by about 0.01 rad whereas the plateau is attained not earlier than 0.035 rad under positive bending and between 0.02 and 0.03 rad under negative bending when the bolts are considered (Fig. 5). This demonstrates that the action of the bolts confers significant ductility to the joint from its opening up to the end of the capacity.

Fig. 18 presents contour plots of the tension hardening variable of the elasto-plastic model used for GCI from the end of the analyses under positive bending. It can be observed that, for tunnel depths of 6 m and 12 m, no tensile plastic strains are occurring at either the intrados of the

circumferential flange or the inner side of the skin, both of which areas were shown to be prone to tensile failure in the analyses with bolts (Fig. 7). The analysis for a tunnel depth of 24 m results in tensile plastic strains of minor significance (less than 0.1%) around the area where the longitudinal and circumferential flanges meet whereas these extend over a larger area and along the intrados of the circumferential flange in the analyses for a tunnel depth of 48 m. Therefore, the results suggest that while yielding in tension can occur when the bolts are removed, the possibility of tensile failure around the longitudinal flange can be ruled out. Undoing the bolts at selected tunnel sections is commonly done when construction works in the proximity of the tunnel are thought to potentially cause damage to the tunnel (Moss & Bowers, 2005) and the numerical results suggest that this can indeed be an effective measure in protecting the flanges from tensile fracturing.

7.2. Effect of bolt preload

The numerical analyses presented so far adopted a bolt preload magnitude corresponding to 25% of the bolt force at yield which was consistent with the laboratory findings reported by Tsiampousi et al. (2017). Nevertheless, variations in the bolt preload at the time of construction of GCI tunnels are to be expected. Therefore the influence of the bolt preload magnitude on the joint rotational behaviour was investigated in a parametric study where bolt preload magnitudes equivalent to 12.5%, 25% and 50% of the bolt force at yield were applied for a tunnel depth of 12 m under positive and negative bending.

Fig. 19 shows the M-θ curves obtained for different bolt preloads. First, it can be seen that the bolt preload magnitude does not affect the magnitude of the bending moment of opening which is consistent with the experimental findings reported by Yu et al. (2017). The influence of the bolt preload only becomes noticeable after a certain amount of rotation which correlates to that at which the bolts are engaged. Thereafter, the M-θ curves reveal a stiffer response for the larger the bolt preload magnitudes with greater differences observed in the analyses under negative bending which is primarily related to the outer and middle bolts becoming active concurrently in this mode. The evolution of bolt forces with rotation is shown in Fig. 20. Under positive bending, the rate at which the forces develop with rotation is greater the smaller the bolt preload values so that the bolt forces from the three analyses tend to converge with rotation contributing to the M-θ curves yielding a similar response at large rotations. Under negative bending, the bolt forces increase at a similar rate for all bolt preloads and so yielding is achieved at smaller rotations for larger bolt preloads, also reflected in the rotation levels at which the ultimate bending moments are attained (Fig. 19b). Tightening the bolts is a common practice as precaution against excessive tunnel deformations caused by nearby construction (Kimmance et al., 1996) and the results presented here suggest that such
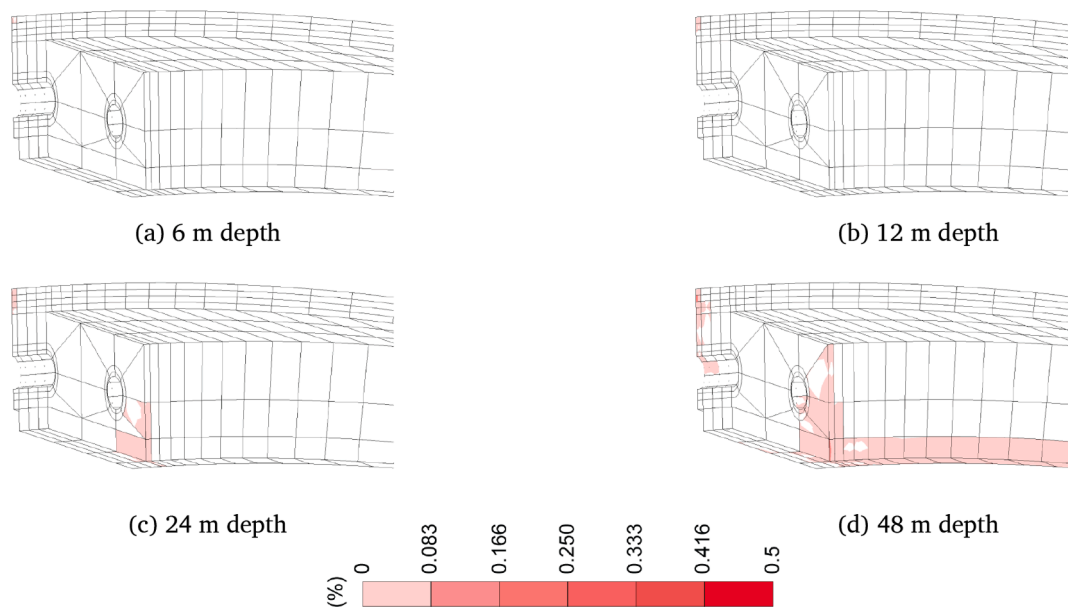
(a) 6 m depth

(b) 12 m depth

(c) 24 m depth

(d) 48 m depth

Fig. 18. Contour plots of the tension hardening variable $\tilde{\varepsilon}_1^p$ of the elasto-plastic model adopted for GCI at the end of the analyses – 11 ft $8^{1/4}$ in (3.562 m) running tunnel geometry without bolts.
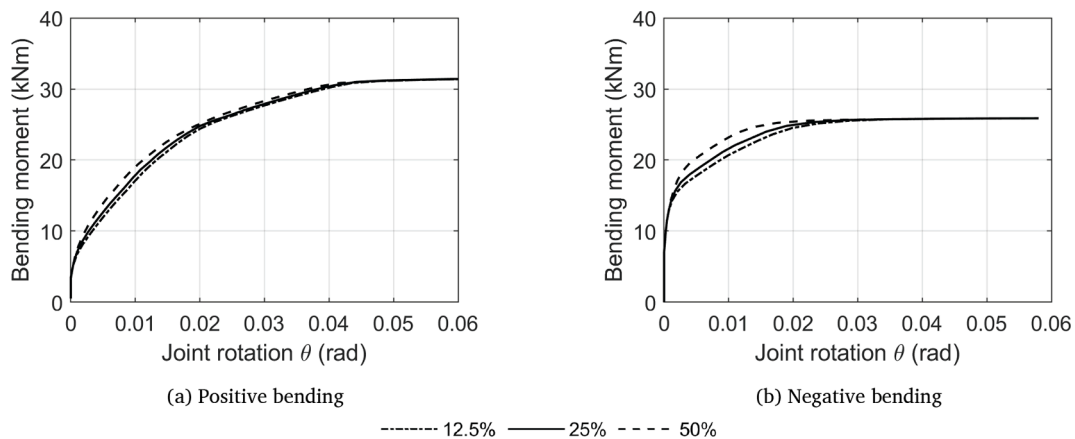

(a) Positive bending

(b) Negative bending

-------- 12.5% ——— 25% - - - - 50%

Fig. 19. Bending moment (kNm) with joint rotation (rad) using different bolt preload forces for a tunnel depth of 12 m – 11 ft $8^{1/4}$ in (3.562 m) running tunnel geometry.

a measure is only likely to be effective in scenarios where some of the joints are opening under negative bending.

7.3. Effect of the out-of-plane boundary condition

The displacements normal to the outer side of the circumferential flange were restricted in the analyses discussed until now. This condition assumes that the presence of adjacent rings prevents any movement of the ring in the longitudinal direction of the tunnel and it is akin to the plane-strain assumption adopted in most tunnelling boundary value problems. As shown in Fig. 2 (right drawings), a deep caulking groove is created between the circumferential flanges of a significant proportion of the GCI tunnels of the LU network and therefore the restriction of the normal displacements all along the height of the flange is not necessarily a precise representation of the actual field condition. To establish the impact of the out-of-plane boundary condition on the rotational behaviour of the joint, the results of analyses performed with the normal displacements restricted only along the height of the skin (denoted subsequently as upper flange fixed) for a tunnel depth of 12 m under positive and negative bending are described and compared with those obtained with the base boundary condition.

Fig. 21 presents the M-θ curves derived from the analyses with different out-of-plane boundary conditions. Under positive bending (Fig. 21a), adopting the upper flange fixed boundary condition results in the same bending moment of opening and ultimate bending moment as those obtained with the full flange fixed boundary condition while a slightly softer M-θ response between rotations of around 0.005 and 0.45 rad is realized with the former boundary condition. The differences between the two analyses can be correlated with Fig. 22a which indicate that, in that range of rotation, the bolt forces develop at a greater rate with the full flange fixed boundary condition. While only minor differences are found between the two boundary conditions under positive bending, they are negligible under negative bending as the M-θ curves (Fig. 21b) and the change in bolt forces are virtually identical in the two analyses (Fig. 22b).

8. Conclusions

The rotational behaviour of longitudinal GCI tunnel joints was characterised numerically with series of 3D analyses. Two joint geometries were considered, these correspond to a running GCI tunnel and a station GCI tunnel. The latter had not been previously investigated
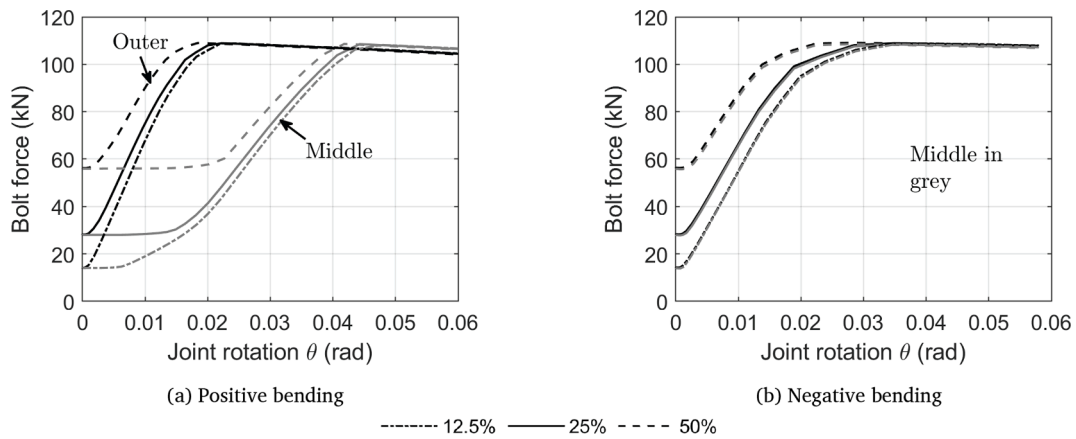
(a) Positive bending   (b) Negative bending

------- 12.5% ——— 25% - - - - 50%

Fig. 20. Bolt force (kN) with joint rotation (rad) using different bolt preload forces for a tunnel depth of 12 m – 11 ft 8$^{1/4}$ in (3.562 m) running tunnel geometry.
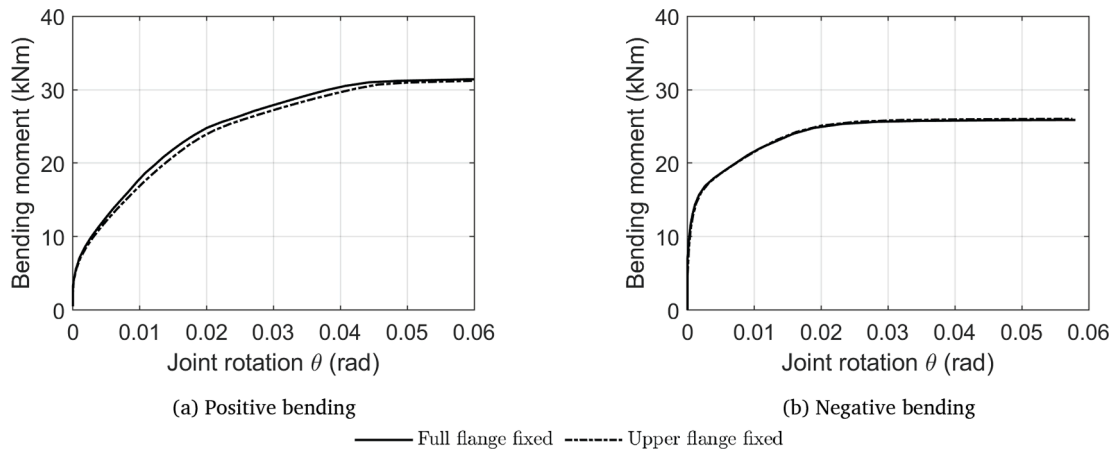

(a) Positive bending   (b) Negative bending

——— Full flange fixed ------- Upper flange fixed

Fig. 21. Bending moment (kNm) with joint rotation (rad) using different out-of-plane boundary conditions for a tunnel depth of 12 m – 11 ft 8$^{1/4}$ in (3.562 m) running tunnel geometry.
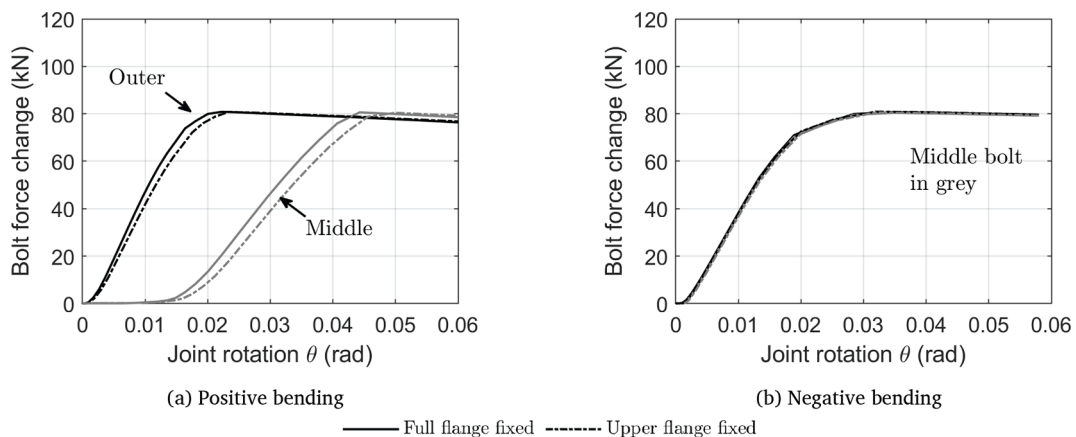

(a) Positive bending   (b) Negative bending

——— Full flange fixed ------- Upper flange fixed

Fig. 22. Change in bolt force (kN) with joint rotation (rad) using different out-of-plane boundary conditions for a tunnel depth of 12 m – 11 ft 8$^{1/4}$ in (3.562 m) running tunnel geometry.

either experimentally or numerically. Their behaviour was evaluated under positive and negative bending subjected to a range of compression levels akin to those experienced at tunnel depths between 6 m and 48 m. The main outcome of the numerical investigation was the derivation of a series of M-θ curves for each bending mode and joint geometry. The results indicate a progressive decay in the joint stiffness from opening up to the ultimate bending moment. As the result of the asymmetry of the joint geometries, the joints exhibit a distinct response under positive and

negative bending; the joints open earlier and exhibit a more ductile response after opening under positive bending. The action of the bolts largely governs the magnitude of the ultimate bending moments and the rotation levels at which those were attained. As a result of their different bolt arrangements, the two joint geometries exhibit a distinct bolt force development with rotation. While some areas of the segment reach the ultimate compressive strength for larger tunnel depths, failure in compression did not generally occur. Under positive bending, the

analyses reveal the potential for tensile failure of GCI at the circumferential flange and the skin adjacent to the longitudinal joint. While this can be observed in both joint geometries, it had a greater impact on the joint response of the running tunnel. The bolt forces in the latter did not fully soften despite extensive areas of GCI experiencing strain-softening and consequently, the magnitude of the ultimate bending moments was close to the maximum joint capacity. The numerical characterisation of the behaviour of the GCI tunnel joints enables the development of new joint models for simplified 2D numerical analysis using structural elements (Ruiz López et al., 2022b).

Additional analyses on the running tunnel geometry demonstrated that while removing the bolts does not significantly affect the point of opening of the joint or the early part of the M-θ curves, it prevents the occurrence of tensile failure of the flange under positive bending. Furthermore, the bolt preload was shown to have negligible effect on the opening of the joint under both bending modes while it does clearly affect the joint stiffness once the bolts are engaged under negative bending. These are useful insights that can be considered in engineering practice when assessing the potential effectiveness of protective measures of the tunnel such as undoing or tightening the bolts prior to new construction in the vicinity of the tunnel. Lastly, the analyses adopting different out-of-plane restraint conditions showed that considering the presence of the deep caulking groove of the circumferential flange has negligible impact on the joint behaviour, particularly under negative bending.

CRediT authorship contribution statement

Agustín Ruiz López: Methodology, Investigation, Formal analysis, Writing – original draft. **Aikaterini Tsiampousi:** Supervision, Writing – review & editing, Funding acquisition. **Jamie R. Standing:** Supervision, Writing – review & editing. **David M. Potts:** Software, Writing – review & editing.

Declaration of Competing Interest

The authors declare that they have no known competing financial interests or personal relationships that could have appeared to influence the work reported in this paper.
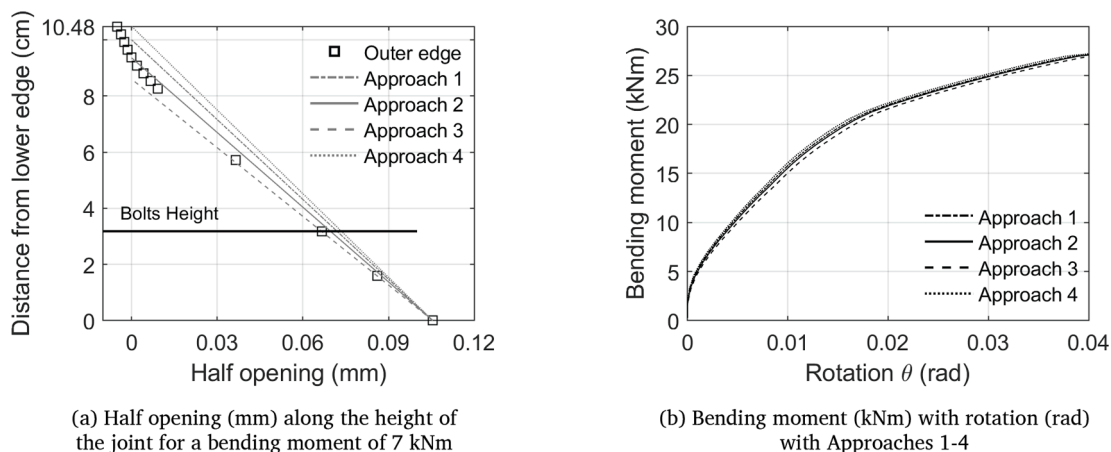
Data availability

We can share all data other than that related to the breakdown of tunnel geometries of the London Underground network

Appendix A. Definition of joint rotation

Once it was established that the rotation of the joint would be taken as that taking place at the outer edge, the geometric procedure to determine the rotation, from the joint displacements given by the FE analysis, had to be decided. This required some judgement since the joint section does not remain completely plane as it rotates due to the interface stiffness restricting the portion of the joint under compression from closing such that an abrupt change on the rotation angle can be observed near the neutral axis, i.e. where the opening is zero. Fig. A1a depicts the half-opening along the height of the joint from one the analyses under positive bending of the 11 ft 8$^{1/4}$ in geometry. It can be observed that while the portion of the section undergoing opening remains approximately plane, the section is bending in the transition from opening to closure. Four different geometric approaches, shown in Fig. A2, to calculate the joint rotation were assessed. The rotation is defined as a straight line connecting the point where maximum opening occurs to a second point that varies depending on the approach adopted. In Approach 1, the second point is taken as that at the closed edge; in Approach 2, the second point is adopted as that at the neutral axis; in Approach 3, the second point is the node closest to that where the opening is maximum; and in Approach 4, the second point is taken as the closed edge assuming that it is the pivot point and so that the opening at that location is zero. The straight lines defined by the four approaches are plotted alongside the numerical data in Fig. A1a. It can be observed that Approach 3 gives the best approximation to the displacements along the portion of the joint that is opening, only missing out slightly the points near the neutral axis. Fig. A1b depicts the M-θ curves obtained with the four approaches for the analysis corresponding to the 11 ft 8$^{1/4}$ in geometry under positive bending for a 6 m tunnel depth. Approach 3 gives the largest rotation throughout the analysis whereas Approach 1 provides the smallest rotation. Overall, only small differences can be observed in the M-θ curves derived with the four approaches. Similar remarks could be made regarding the comparison between the four approaches under negative bending. Ultimately, as explained in Section 5, it was decided to employ Approach 3 to calculate the rotation in all the analyses presented in this paper.

(a) Half opening (mm) along the height of the joint for a bending moment of 7 kNm

(b) Bending moment (kNm) with rotation (rad) with Approaches 1-4

Fig. A1. Comparison of different approaches to calculate the joint rotation under positive bending – 11 ft 8$^{1/4}$ in (3.562 m) tunnel joint geometry for a 6 m tunnel depth.
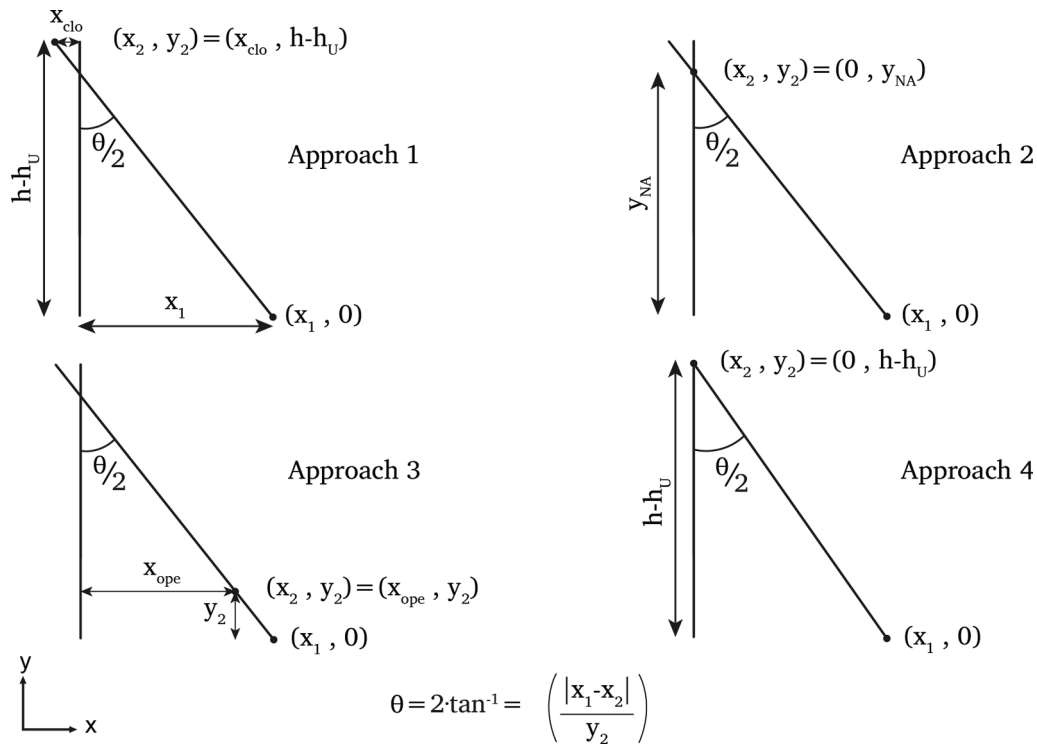
Fig. A2. Outline of the four approaches to calculate joint rotation.

Appendix B. Mesh sensitivity analyses

The response of the tunnel joint is assessed here adopting the two FE mesh discretisations, corresponding to the joint of the 11 ft $8^{1/4}$ in tunnel geometry, shown in Fig. B1. 'Mesh a' was employed in the numerical analyses discussed in Section 6.1 whereas 'Mesh b' was utilised in those presented in Section 7. The analysis results corresponding to a tunnel depth of 12 m under both positive (without strain-softening) and negative bending are presented below.

Fig. B2 shows the rotational response of the joint, in terms of M-θ curves and bolt force-rotation curves, under positive bending for the two mesh discretisations. Negligible differences can be observed between the two results in relation to the M-θ curves while minor ones are noticed in terms of the change in bolt forces. Similarly, Fig. B3 presents the joint

(a) Mesh a

(b) Mesh b

Fig. B1. Finite element meshes investigated in the sensitivity study.

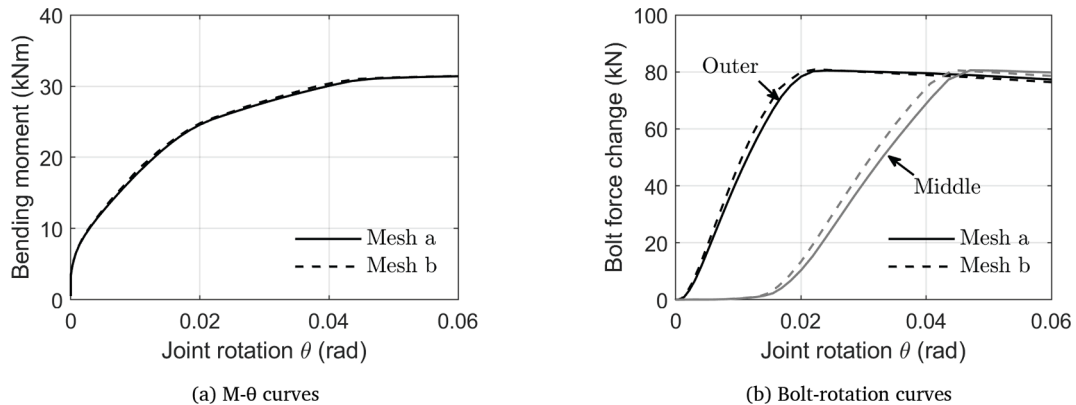
(a) M-θ curves

(b) Bolt-rotation curves

Fig. B2. Rotational response of the 11 ft $8^{1/4}$ in (3.562 m) tunnel joint geometry for a 12 m tunnel depth under positive bending with different meshes.
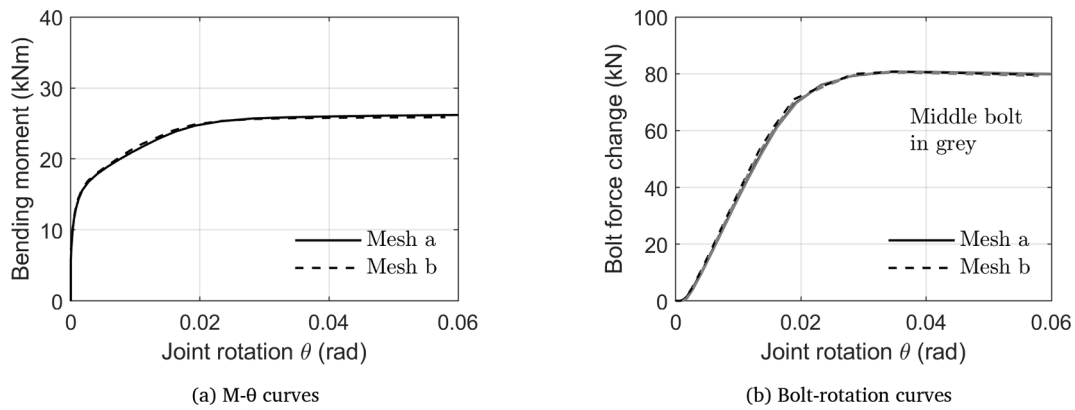
(a) M-θ curves

(b) Bolt-rotation curves

Fig. B3. Rotational response of the 11 ft 8$^{1/4}$ in (3.562 m) tunnel joint geometry for a 12 m tunnel depth under negative bending with different meshes.

response under negative bending. It can be observed that negligible differences are observed between the results obtained with the two meshes. From these results, it can be concluded that the joint response obtained with 'Mesh b' is essentially equivalent to that realised with 'Mesh a'.

References

Afshan, S., Yu, J., Standing, J., Vollum, R., Potts, D., 2017. Ultimate capacity of a segmental grey cast iron tunnel lining ring subjected to large deformations. Tunn. Undergr. Space Technol. 64, 74–84.

Blom, C., 2002. Design philosophy of concrete linings for tunnels in soft soils. TU Delft, Delft University of Technology. PhD thesis.

Bradley, W., Srinivasan, M., 1990. Fracture and fracture toughness of cast irons. Int. Mater. Rev. 35 (1), 129–161.

Day, R.A., Potts, D.M., 1994. Zero thickness interface elements—numerical stability and application. Int. J. Numer. Anal. Meth. Geomech. 18 (10), 689–708.

GCG, 2002. The assessment of running tunnel linings. Prepared for INFRACO JNP Ltd. Draft Final Report. Technical report. Tube Lines document reference: GCG-L001-N369- DTAAWP1-TUN-RPT-00001.

Hillerborg, A., Modéer, M., Petersson, P.-E., 1976. Analysis of crack formation and crack growth in concrete by means of fracture mechanics and finite elements. Cem. Concr. Res. 6 (6), 773–781.

Hordijk, D., Gijsbers, F., 1996. Laboratoriumproeven tunnelsegmenten. Reporte Interno K100-W-026, TNO-Bouw, Delft.

Irwin, G.R., 1957. Analysis of stresses and strains near the end of a crack traversing a plate. J. Appl. Mech. 24, 361–364.

Janssen, P., 1983. Tragverhalten von Tunnelausbauten mit Gelenktübbings. Technischen Universitat Carolo-Wilhelmina. PhD thesis.

Jin, Y., Ding, W., Yan, Z., Soga, K., Li, Z., 2017. Experimental investigation of the nonlinear behavior of segmental joints in a water-conveyance tunnel. Tunn. Undergr. Space Technol. 68, 153–166.

Kimmance, J. P., Lawrence, S., Hassan, O., Purchase, N. J., Tollinger, G., 1996 Observations of deformations created in existing tunnels by adjacent and cross cutting excavations. In: Mair, R. J., Taylor, R. N. (Eds.) Geotechnical Aspects of Underground Construction in Soft Ground: Proceedings of the International Symposium. Taylor Francis Group, Rotterdam, 707-712.

Li, X., Yan, Z., Wang, Z., Zhu, H., 2015. A progressive model to simulate the full mechanical behavior of concrete segmental lining longitudinal joints. Eng. Struct. 93, 97–113.

Li, Z., Soga, K., Wang, F., Wright, P., Tsuno, K., 2014. Behaviour of cast-iron tunnel segmental joint from the 3D FE analyses and development of a new bolt-spring model. Tunn. Undergr. Space Technol. 41, 176–192.

Moss, N., Bowers, K., 2005. The effect of new tunnel construction under existing metro tunnels. In: Bakker et al. (Eds.) Geotechnical Aspects of Underground Construction in Soft Ground: Proceedings of the International Symposium. Taylor Francis Group, Amsterdam, 151-157.

Potts, D.M., Zdravkovic, 1999. Finite element analysis in geotechnical engineering: theory. Thomas Telford, London.

Ruiz López, A. D., 2022. Development of advanced numerical models for grey cast iron tunnel linings. PhD Thesis. Imperial College London.

Ruiz López, A., Tsiampousi, A., Standing, J.R., Potts, D.M., 2022a. Numerical investigation of a segmental grey cast iron tunnel ring: validation with laboratory data and application to field conditions. Comput. Geotech. 141, 104427.

Ruiz López, A., Tsiampousi, A., Standing, J.R., Potts, D.M., 2022b. A new model for simulating the behaviour of grey cast iron tunnel joints with structural elements. Submitted for publication.

Schütz, R., 2010. Numerical modelling of shotcrete for tunnelling. Imperial College London. PhD thesis,.

TfL, 2020. Personal communication (email).

Thomas, H., 1974. Tunnelling in London Clay: A study with field investigations including the long term structural behaviour of two linings. University of Surrey. MPhil Thesis,.

Thomas, H., 1977. Measuring the structural performance of cast iron tunnel linings in the laboratory. Ground Eng. 10, 29–36.

Tsiampousi, A., Yu, J., Standing, J., Vollum, R., Potts, D., 2017. Behaviour of bolted cast iron joints. Tunn. Undergr. Space Technol. 68, 113–129.

Tvede-Jensen, B., Faurschou, M., Kasper, T., 2017. A modelling approach for joint rotations of segmental concrete tunnel linings. Tunn. Undergr. Space Technol. 67, 61–67.

Ward, W., Thomas, H., 1965. The development of earth loading and deformation in tunnel linings in London Clay. In: Proceedings of the Sixth International Conference on Soil Mechanics and Foundation Engineering, 1965, vol. 2, 432–436.

Yu, J., Standing, J., Vollum, R., Potts, D., Burland, J., 2017. Experimental investigations of bolted segmental grey cast iron lining behaviour. Tunn. Undergr. Space Technol. 61, 161–178.